Discrete Distances Applied to 2D Granulometry and 3D Reconstruction

A. Montanvert and Y. Usson

Lab. TIMC - IMAG
CERMO - BP 53X
38041 GRENOBLE cedex - FRANCE

Abstract

In this paper, we present some particular aspects of discrete distances. The efficiency of chamfer distances in two-dimensional (2D) and three-dimensional (3D) image analysis is demonstrated for two applications.

Chamfer distances are computed in $O(N^2)$ time, and have some properties related to discrete space. They are often used to extract features, or to build medial lines. The first application is a granulometry for the study of materials in which size distributions are computed from image distance. The second application is a 3D reconstruction from cross-serial sections: this process is based on the computation of a fate map from distance images which provides the voxel structure of the inferred object.

1 Introduction

In image processing, it is necessary to represent and describe two and three dimensional shapes. Because images are discrete (matrix of pixels), coded with integer values, and are usually processed on sequential computers, many approaches work directly on discrete space. Here we have used discrete distances, in particular the chamfer distances, which belong to the field of digital geometry (Section 2).

Chamfer distances are computed in $O(N^2)$ time for a NxN image, and can approximate the Euclidean distance very well. Moreover, chamfer distances have specific properties in discrete space. Distances also lead to medial lines and are frequently used for shape splitting or shape approximations.

The efficiency of chamfer will be shown here for two applications. The first is the computation of granulometry for study of materials (Section 3). Dilation and erosion are easily extracted from the distance image. The size distributions of pores inside a material are computed using chamfer distances. The results are compared to the usual granulometry by using mathematical morphology. The second application is a strategy for reconstructing three dimensional objects from serial cross-sections (Section 4). Here a fate map is defined from the sections of the two extremities. This fate map is an image in which each pixel is assigned to a birth date or a death date deduced from a distance image computed from the difference between the two images. The results show the efficiency and quality of the method on real applications in medicine.

2 Discrete Distances

2.1 Chamfer distances

Given a binary image A, a distance image is such that each pixel of the objects (connected components) is assigned to its distance from the background. The basic distances are the City Block distance (d_4) and the Cheesboard distance (d_8) [1] ; for two points $P(i_P, j_P)$ et $Q(i_Q, j_Q)$, d_4 and d_8 are defined by:

$$d_4 (P, Q) = |i_P - i_Q| + |j_P - j_Q|$$
$$d_8 (P, Q) = \max (|i_P - i_Q| , |j_P - j_Q|)$$

These distances differ from the Euclidean distance d_E, but they are the basis of the sequential algorithm, efficient on usual sequential computers and which generates integer values [2]. These distances are called chamfer distances, because the shape of the discrete disks that they generate are polygons. We do not use the Euclidean distance transform which requires storage of the displacements along the two axes [3], because the algorithm is not so simple and elegant, or it needs some special data structures [4].

A chamfer distance is defined by a $(2u+1)^2$ kernel (noted ker_u, in which the visible points, associated with the Farey serie of order u, are assigned to weights defined by the Euclidean distance: ker_u (h,k) means that the distance from the point (i,j) to the point (i+h, j+k) is equal to ker_u (h,k).

The optimal kernels for a (3x3) and (5x5) neighborhood are given below:

$$ker_1 = \begin{pmatrix} 4 & 3 & 4 \\ 3 & 0 & 3 \\ 4 & 3 & 4 \end{pmatrix} \qquad ker_2 = \begin{pmatrix} . & 11 & . & 11 & . \\ 11 & 7 & 5 & 7 & 11 \\ . & 5 & 0 & 5 & . \\ 11 & 7 & 5 & 7 & 11 \\ . & 11 & . & 11 & . \end{pmatrix}$$

To compute the distance image, the kernel is split into $ker_{u, forward}$ and $ker_{u, backward}$. For example:

$$ker_{1, forward} = \begin{pmatrix} 4 & 3 & 4 \\ 3 & 0 & \end{pmatrix} \qquad ker_{1, backward} = \begin{pmatrix} & 0 & 3 \\ 4 & 3 & 4 \end{pmatrix}$$

Then the image distance is computed in $O(N^2)$ times as follows:

Forward scanning:
for i = 1 to N do   for j = 1 to N do
A(i,j) = min $_{(h,k)}$ (A (i+h, j+k) + ker. $_{u, forward}$ (h,k)) ;

Backward scanning:
for i = N to 1 do   for j = N to 1 do
A(i,j) = min $_{(h,k)}$ (A (i+h, j+k) + ker $_{u, backward}$ (h,k)) ;

When the size of the kernel increases, the error with respect to d_E can be decreased. For instance, the relative maximum error with respect to d_E can be reduced to [5]:

- 41.42% for d_4, 29.29% for d_8, 5.72% for d_{3-4}, in a 3x3 kernel;
  - 1.98% for d_{5-7-11}, in a 5x5 kernel;
  - 1.38% for $d_{12-17-°-38-43}$, in a 7x7 kernel;
  - and even 0.47% in a 11x11 kernel.

The choice of the weights in the kernel depends on an optimization criterion evaluated in comparison with d_E, and to several constraints in order to ensure that the resulting chamfer distance is a distance (reflexive, symmetrical and transitive) [5].

The main advantage of enlarging the kernel is that the chamfer distance becomes robust under rotation, which is necessary in many applications.

			3	3	3	3	3	3										
			3	6	6	6	6	3										
	3	3	3	4	7	9	9	6	3									
	3	6	6	7	8	11	9	6	3									
	3	6	9	10	11	12	10	7	4	3								
3	4	7	10	13	14	14	11	8	7	4	3	3	3	3	3	3	3	3
3	6	8	11	14	16	15	12	11	8	7	6	6	6	6	6	4	3	3
3	6	8	11	12	15	16	15	12	11	10	9	9	8	7	4	3		
3	4	7	8	11	14	16	16	15	14	13	12	10	7	4	3			
	3	4	7	10	12	14	15	16	16	14	11	8	6	3				
		3	6	8	10	11	12	15	15	12	10	7	4	3				
			3	4	6	7	8	11	12	12	11	8	6	3				
				3	3	4	7	8	9	9	9	8	7	4	3			
					3	4	6	6	6	6	6	4	3					
						3	3	3	3	3	.3	3						

Figure 1. Distance image for d_{3-4}.

In sections 3 and 4, we will limit ourselves to the use of d_{3-4} (see Fig. 1), and d_{5-7-11} (see Fig. 2) and we show that they already provide excellent results.

			5	5	5	5	5	5										
				5	10	10	10	10	5									
		5	5	5	7	11	15	15	10	5								
		5	10	10	11	14	18	15	10	5								
		5	10	15	16	18	21	16	11	7	5							
5	7	11	16	21	22	22	18	14	11	7	5	5	5	5	5	5	5	
5	10	14	18	22	27	25	21	18	14	11	10	10	10	10	10	7	5	5
5	10	14	18	21	25	29	25	21	18	16	15	15	14	11	7	5		
5	7	11	14	18	22	27	29	25	22	21	20	16	11	7	5			
	5	7	11	16	21	22	25	28	27	22	18	14	10	5				
		5	10	14	16	18	21	25	25	21	16	11	7	5				
			5	7	10	11	14	18	20	20	18	14	10	5				
				5	5	7	11	14	15	15	14	11	7	5				
					5	7	10	10	10	10	7	5						
						5	5	5	5	5	5							

Figure 2. Distance image for d_{5-7-11}.

2.2 Use of discrete distances

Distance images are very useful in image processing, and we give a few examples in this section. One of the best known fields of application is the extraction of medial axes for shape coding [6], or medial lines for shape description and shape splitting of aggregates [7,8].

Feature extraction is also of primary interest, because features can intregrate distance images in 2D [9] and in 3D [10]. Distances are also used in shape approximation [11], shape matching in 2D space [12] or 3D space [13] and hierarchical description of shape [14].

Distance images were also used in robotics to represent the configuration space of an "arm robot" and to compute its trajectory [15].

3 Granulometry

3.1 Image analysis and granulometry

Granulometry is used in the study of materials, such as sand, pebbles or cellular phases of components, to characterize the size distribution of the particules inside a material. Processed by hand, the elements are sorted, for instance, through a riddle and then counted or weighted.

In fact granulometry is not confined to only counting particles because it can be extended to features and then to images representing elements which are not disconnected [16].

A granulometry on a set X is represented by a normalized distribution function defined by:

$G(\mu) = [Meas(X) - Meas(T_\mu(X))] / Meas(X)$, where *Meas* is the chosen measure and T_μ the transformation applied on X. The associated density function is given by:

$$g(\mu) = G'(\mu) \quad or \quad G(\mu) = \int_0^\mu g(\mu).d\mu$$

We are interested in measuring surfaces by granulometry. Using image analysis, we deal with

granulometry by opening, which involves mathematical morphology operators [17].

Then *Meas* is the measure of areas in the image, and T_μ is an opening with a structuring element of radius μ; the structuring element must be convex to ensure that the granulometry is correct.

Granulometry is computed by repeatedly applying openings with structuring elements which are circles of increasing radius. These operations are time consuming when computed on a sequential computer.

3.2 The use of chamfer distances

On an image distance, we know for each point its distance to the background; this is sufficient to efficiently compute opening operations. More presisely, a chamfer disk is a polygon (an octogon for $d_{3\text{-}4}$, and a hexadecagon for $d_{5\text{-}7\text{-}11}$), that we will use as approximations of the Euclidean disk (see Fig. 3).
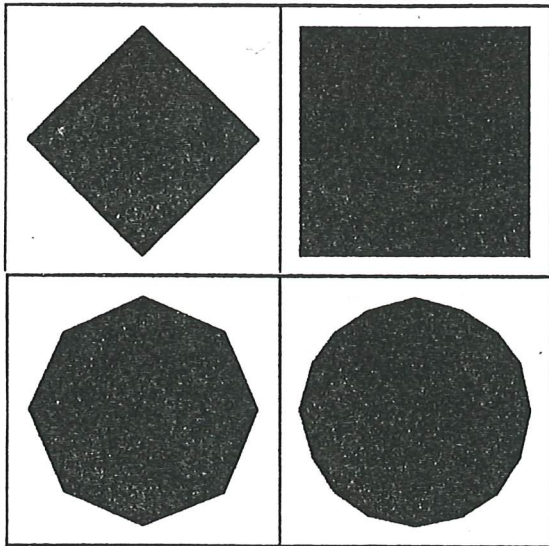
Figure 3. Discrete disks for d_4, d_8, $d_{3\text{-}4}$, $d_{5\text{-}7\text{-}11}$.

An opening is an erosion followed by a dilation. The eroded set of X is the location of points x of X such that the structuring element centered on x is included in X.

Consequently, using a chamfer disk of radius R, the eroded set of X is the subset of X whose distance to the background is greater than ß.R, where ß=3 for $d_{3\text{-}4}$, and ß=5 for $d_{5\text{-}7\text{-}11}$.

The dilated set of X is the location of points x for which the structuring element centered on x intersects X. This is equivalent to saying that it is the union of disks whose center is in X; so we simply have to define the disks centered on contour points.

Using chamfer distances, the disks can be computed efficiently by taking into account the properties of these distances. For instance, in the first octant, for P(x,y) [5]:

$d_{3\text{-}4}(0,P) = 3x+y;$
$d_{5\text{-}7\text{-}11}(0,P) = 5x+y$ if $x \geq 2y$
and $d_{5\text{-}7\text{-}11}(0,P) = 4x+3y$ if $x < 2y$.

These properties of chamfer disks speed up the computation process for dilation.

Then the chamfer opening of radius R of an image A is computed as follows (see Fig. 4):
- compute $\mathcal{DT}^A$, the chamfer distance image of A;
- for each pixel (i,j) with a non zero value:
- if $\mathcal{DT}^A(i,j) > ß.(R+1)$ then (i,j) is in the opening set else if $\mathcal{DT}^A(i,j) > ß.R$ then the chamfer disk centered on (i,j) is in the opening set.
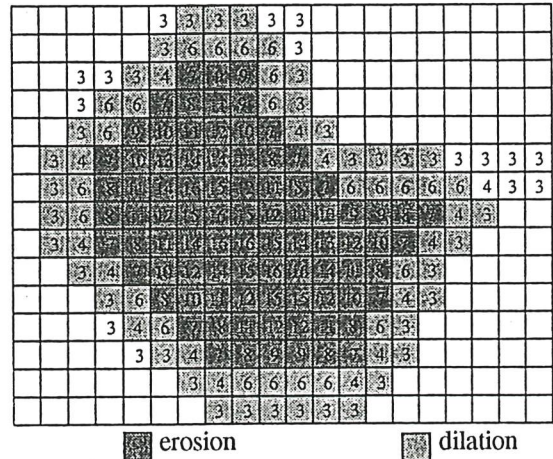

🔲 erosion   🔲 dilation

Figure 4. Opening as erosion and dilation for $d_{3\text{-}4}$, with R=2.

3.3 The results on material studies

The method described in §3.2 has been applied to the study of the porous phase of an autoclaved aerated concrete (AAC) and to characterize various materials (see Fig. 5).
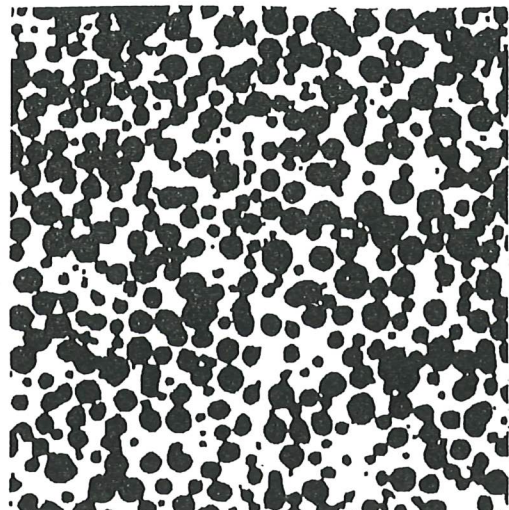

Figure 5. Material: polished section of AAC.

For instance AAC samples are impregnated by a black dye epoxy resin, then the two main classes of the porous phase (a microporous structure in the solid matrix and a macroporous cellular structure of air bubbles) can be distinguished. The size of air bubbles allows direct observation by optical microscopy and characterization of the cellular porous phase.

We compared the results of mathematical morphology and 3-4 chamfer on density function and distribution function. The resulting functions are shown in Figure 6 and 7. The latter provides some results close to the former, and the computation time is smaller by an order of magnitude: developed on a Apollo-HP computer, the chamfer methods takes 2 minutes on a 512x512 image, while more than one hour is necessary with the other approach.

Radius	Distribution Function		
	Circle	Octogon	Hexadecagon
0	0.0000	0.0000	0.0000
1	0.0028	0.0037	0.0037
2	0.0107	0.0133	0.0133
3	0.0249	0.0306	0.0306
4	0.0418	0.0585	0.0507
5	0.0733	0.0858	0.0858
6	0.1020	0.1201	0.1201
7	0.1569	0.1935	0.1935
8	0.2448	0.3047	0.2855
9	0.3407	0.3808	0.3679
10	0.4550	0.4772	0.4798
11	0.5315	0.5792	0.5790
12	0.6557	0.7474	0.7058
13	0.8108	0.8336	0.8318
14	0.8934	0.9064	0.9053
15	0.9402	0.9535	0.9470
16	0.9782	0.9937	0.9808
17	0.9922	0.9940	0.9934
18	1.0000	1.0000	1.0000

Figure 6. Density and distribution functions for AAC using mathematical morphology.
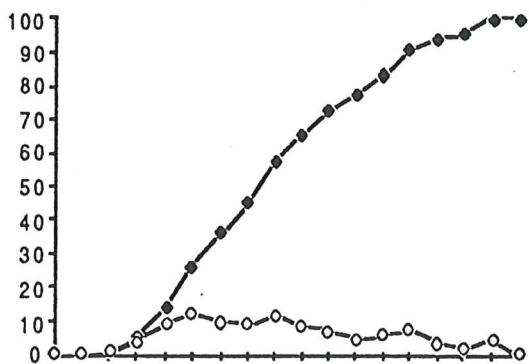

Figure 7. Density and distribution functions for AAC using chamfer distance d_{3-4}.

To improve the quality of the results, we decided to use 5-7-11 chamfer. We show in Figure 8 the comparison of the opening by mathematical morphology, and then using 3-4 and 5-7-11 chamfer.

One more advantage of chamfer distances, is that the result is not influenced by the border of the image. These tools were used to provide mesures in several projects of material studies, and some characteristics were derived.
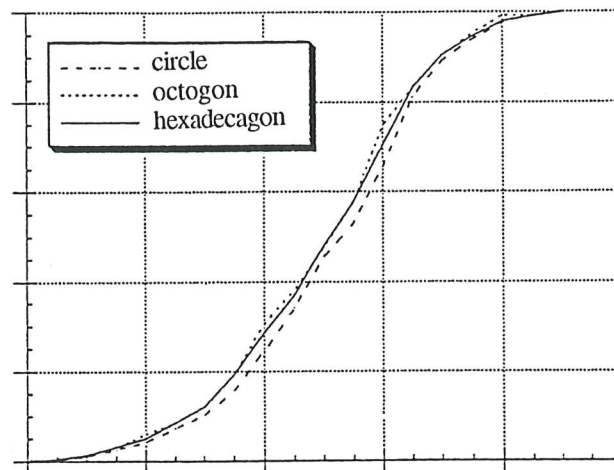

Figure 8. Distribution functions and their representations for AAC using mathematical morphology (circle), d_{3-4} (octogon) and d_{5-7-11} (hexadecagon).

4 Three-dimensional reconstruction

4.1 Overview of methods

Three-dimensional reconstruction is necessary in many applications in biology and medecine when a 3D object is simply known by a limited number of slices. We consider the case in which the slices are parallel cross-sections. The resulting images are segmented into binary images.

In general the distance between the sections is greater than the sampling distance in the section plane. This is due to mechanical constraints in the case of physical sections (the material between sections is destroyed by a knife) or it is inherent to the properties of the imaging

system (lesser resolution along the optical axis of a confocal microscope).

Our target is to infer the missing slices between each pair of images. We can restrict ourselves to the case of two images, one from each extremity. Each of these images contains the connected components associated with the slices of the 3D object.

The classical methods are based on the association of these connected components two by two between the two images. Then two approaches can be used.

The usual approach is to build a facet model of object surface: during two simultaneous contour followings, elementary triangles are defined, which take into account some optimality criteria on local curvature, area... [18, 19]. The expected surface can also be associated with a tetrahedrisation of the space, based on the Delaunay triangulation of the contours, to which vertices are added [20].

We previously developed a method which builds the intermediate volume by using a representation by weighted skeletons of the extremities: the corresponding medial line graphs are matched and intermediate graphs computed, each providing a new slice [21].

The main disadvantage of these methods is that the extraction and the association of the images of the extremities are necessary, requiring a tricky preprocessing of the slices. Consequently these techniques cannot work when the topology of the slices is complex, which is most often the case in real applications, such as reconstruction of human organs in medicine.

4.2 Inference of missing data based on distance transformation

The method proposed here has been developed in a voxel environment and gives satisfactory results as long as there is a high degree of overlap between structures in two consecutive sections. If we consider A and B to be the binary images of two consecutive sections, some structures in A intersect some structures in B and some do not. During the inference process from A to B the shape of some structures will have to be gradually transformed, others will have to appear or to disappear.

Therefore, we can define a different **destiny** or fate for all the structures and *in extenso* for their smallest elements, the pixels. Our algorithm consists in building a **fate map** of the pixels which is then used to reconstruct each inferred section.

A pixel is given a fate depending on the combination of its presence or absence in A and B, respectively. A pixel missing in A but present in B will have to appear (birth) during the inference. A pixel present in A but missing in B will have to disappear (death). A pixel which is both present or both missing in A and B will be left unchanged.

The next step consists in defining the so-called **date of birth** and **date of death** for those pixels that are to be changed during inference. These dates are derived from the distance transforms of A and B. For a pixel which is bound to appear or disappear the date is the resultant of the shortest distances to the closest edge in A and to the closest edge in B. This condition insures that there is a gradual change of shape from A to B since the respective influences of edges in A and B is modulated as a function of the distance to these edges.

Detailed formalization

Let A and B be two binary images, where $\mathcal{L}^A = \left\{ \lambda_1^A, ..., \lambda_p^A \right\}$ and $\mathcal{L}^B = \left\{ \lambda_1^B, ..., \lambda_q^B \right\}$ are the sets of the connected components of A and B, respectively.

$\mathcal{A}_1$ and $\mathcal{A}_2$ are two subsets of $\mathcal{L}^A$ defined as follows:

$$\mathcal{A}_1 = \left\{ \lambda_n^A \in \mathcal{L}^A \, / \, \lambda_n^A \cap B \neq \varnothing \text{ and } \lambda_n^A \not\subset B \right\}$$

$$\mathcal{A}_2 = \left\{ \lambda_n^A \in \mathcal{L}^A \, / \, \lambda_n^A \subset \overline{B} \right\}$$

$\mathcal{B}_1$ and $\mathcal{B}_2$ are two subsets of L^B defined as follows:

$$\mathcal{B}_1 = \left\{ \lambda_n^B \in \mathcal{L}^B \, / \, \lambda_n^B \cap A \neq \varnothing \text{ and } \lambda_n^B \not\subset A \right\}$$

$$\mathcal{B}_2 = \left\{ \lambda_n^B \in \mathcal{L}^B \, / \, \lambda_n^B \subset \overline{A} \right\}$$

The fate $Fate^{A \rightarrow B}$ of a pixel (i,j) during the process of inference from A to B is given by:

$$Fate_{ij}^{A \rightarrow B} = \begin{cases} \text{birth} & \text{if } (i,j) \in \overline{A} \cap B \\ \text{death} & \text{if } (i,j) \in A \cap \overline{B} \\ \text{survival} & \text{if } (i,j) \in A \cap B \\ \text{nil} & \text{if } (i,j) \notin A \cup B \end{cases}$$

$Fate_{ij}^{A \rightarrow B}$, date of birth =

$$\begin{cases} \dfrac{\mathcal{DT}_{ij}^{\overline{A}}}{\mathcal{DT}_{ij}^{\overline{A}} + \mathcal{DT}_{ij}^{B}} & \text{if } (i,j) \in \overline{A} \cap \mathcal{B}_1 \qquad (1) \\[4ex] \text{else} \\[2ex] \alpha \left(1 - \dfrac{\mathcal{DT}_{ij}^{\mathcal{B}_2}}{\max \left[\mathcal{DT}^{\mathcal{A}_2}, \mathcal{DT}^{\mathcal{B}_2} \right]} \right) & \text{if } (i,j) \in \mathcal{B}_2 \qquad (2) \end{cases}$$

The date of birth of a pixel (i,j) is given by the

distance from the closest edge in A weighted by the sum of the distances from the closest edges in A and B (formula 1), or it is given by the distance from the closest edge in image B (formula 2). The weighting terms control the smooth transformation of shape between A and B.

The date of death of a pixel (i,j) is given by similar formulas (3) and (4) which correspond to the transformation of the shape from A to B.

$$Fate_{ij}^{A \to B}, \text{ date of death} =$$

$$\begin{cases} \dfrac{\mathcal{DT}_{ij}^{A}}{\mathcal{DT}_{ij}^{A} + \mathcal{DT}_{ij}^{\overline{B}}} & \text{if } (i,j) \in \mathcal{A}_1 \cap \overline{B} \quad (3) \\[4mm] \text{else} \\[2mm] \dfrac{\alpha \ \mathcal{DT}_{ij}^{\mathcal{A}_2}}{\max \left[\mathcal{DT}^{\mathcal{A}_2}, \mathcal{DT}^{\mathcal{B}_2} \right]} & \text{if } (i,j) \in \mathcal{A}_2 \quad (4) \end{cases}$$

where α is an arbitrary coefficient ranging from 0 to 1.

Finally, the value of a given pixel (i,j) in the kth inferred image I is:

$$I_{ij}^{k} = \begin{cases} 1 & \text{if } (i,j) \in \overline{A} \cap B \text{ and } \dfrac{k}{k_{\max}} \geq Fate_{ij}^{A \to B} \\[3mm] 0 & \text{if } (i,j) \in \overline{A} \cap B \text{ and } \dfrac{k}{k_{\max}} < Fate_{ij}^{A \to B} \\[3mm] 0 & \text{if } (i,j) \in A \cap \overline{B} \text{ and } \dfrac{k}{k_{\max}} \geq Fate_{ij}^{A \to B} \\[3mm] 1 & \text{if } (i,j) \in A \cap \overline{B} \text{ and } \dfrac{k}{k_{\max}} < Fate_{ij}^{A \to B} \\[3mm] 1 & \text{if } (i,j) \in A \cap B \\[1mm] 0 & \text{if } (i,j) \notin A \cup B \end{cases}$$

where k is the inference order such as $0 \geq k \geq k_{\max}$ and $k_{\max}$ the maximum number of images to be inferred.

4.3   Results

Two examples illustrate our approach, the first example uses synthetic data and the second example shows the application to a real case.

The trousers example

The starting section contains a large circular shape and the end section contains two smaller circular shapes. The latter overlap the shape in the starting section. Figure 9 shows the fate map that is used for the inference of missing sections. The bottom part of Fig.9 shows three different views of the reconstruction with 100 inferred sections. The reconstructed object mimics a pair of trousers where the starting section corresponds to the belt and the end section corresponds to the cuffs. It can be seen

that the junction of the legs is shaped like an arch, illustrating that the change between the starting and ending shapes is continuous and moreover smooth.
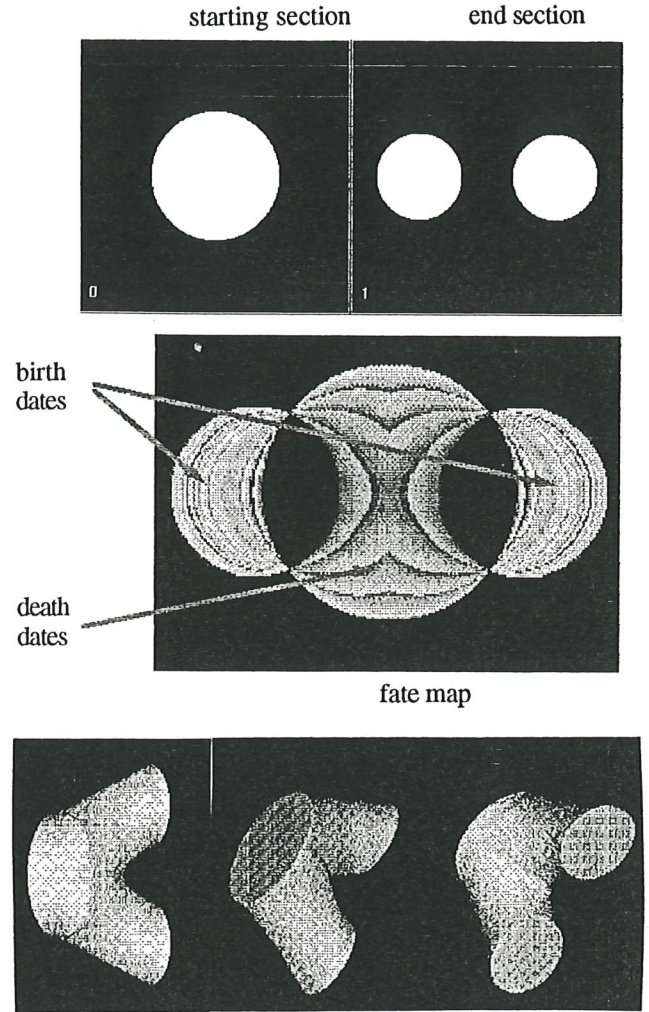

starting section   end section

birth dates

death dates

fate map

three views of the inferred volume

Figure 9. Inference of missing data.
Synthetic example.

Human fetal heart example

This example is the application of our algorithm to real data. In this case, these are the venticles of the heart of human fetus.

There are 22 physical slices and the distance between two slices is 12 fold the distance between pixels in the binary images. Figure 10 shows the series of inferred sections (numbered 24 to 35) between the original slices 2 and 3. Figure 11 left column shows two views of the reconstruction obtained without inference. In this case the voxels are elongated 12 fold along the z axis and the result strongly resembles a staircase, in particular when the angle of view is orthogonal to the z axis (bottom view).
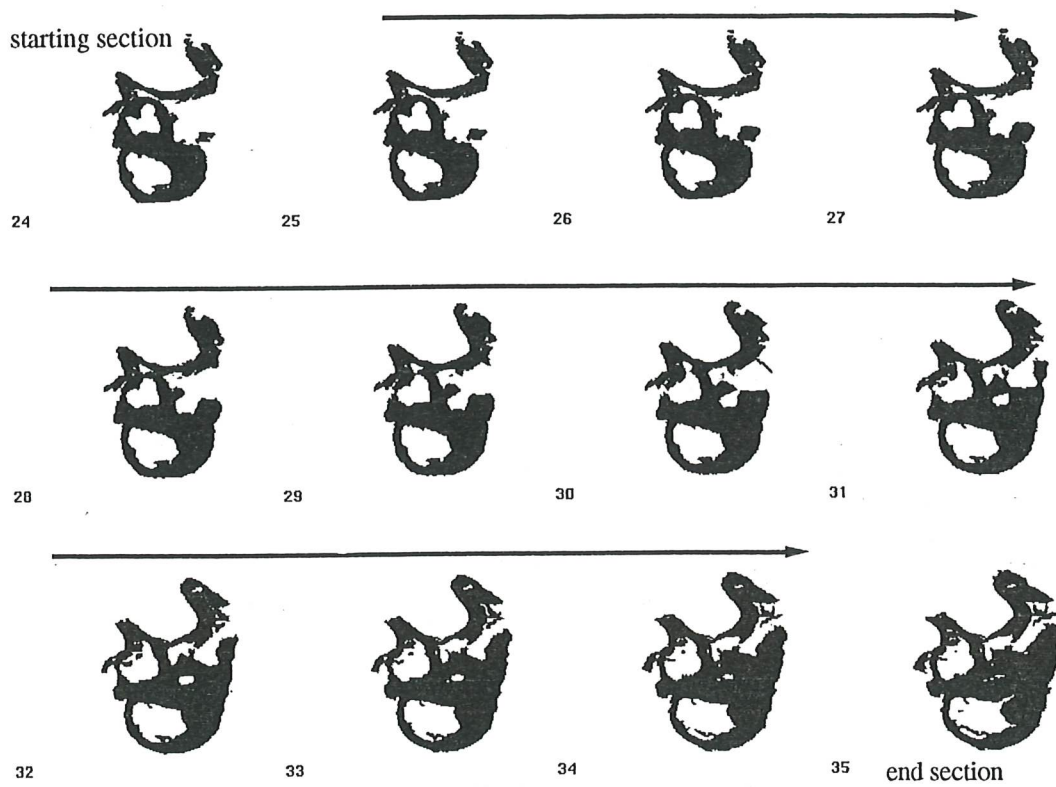
starting section

24   25   26   27

28   29   30   31

32   33   34   35   end section

Figure 10. Series of 12 inferred sections: human fetal heart.
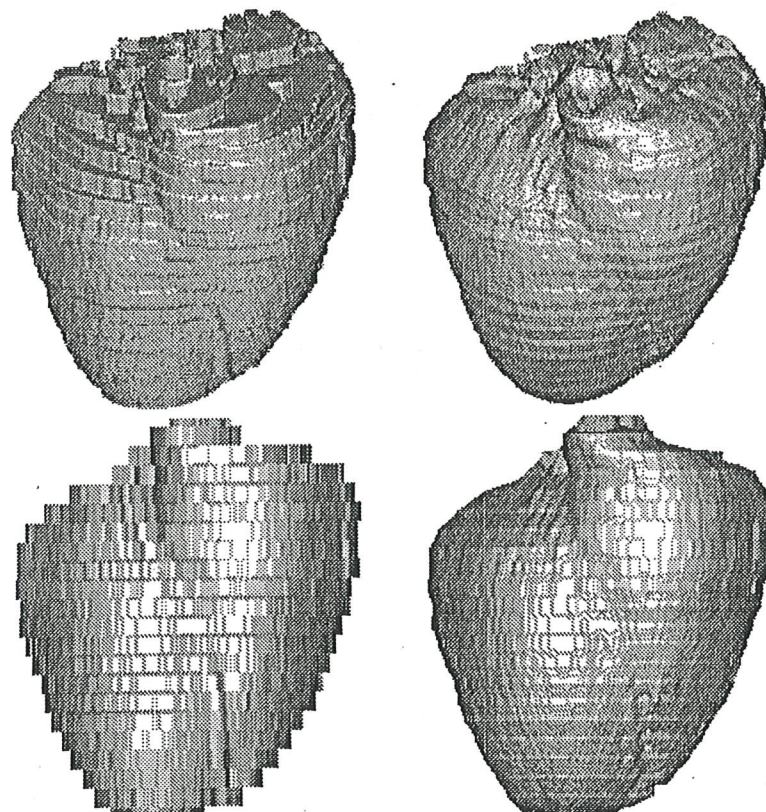
Figure 11. Reconstructions of human fetal heart. Left: raw data, Right: inferred data.

Figure 11 right column shows two views of the reconstruction obtained after inference. Here the voxels are cubical and the obtained result is very realistic. In fact, when the reconstruction after inference is compared with photographs of the heart taken before it was cut, no obvious differences are visible.

5 Conclusion

The introduction of discrete distances in various application fields has proved to be efficient. The major gain is the drastic reduction of computation time, mainly because the methods do not imply either iterative or combinatorial calculation and are straightforward. They are easy to implement on sequential computers.

The distance image can also be used to characterize the distribution of connections of pores or to evaluate a thermal conductivity of a material [22].

The inference of sections by our method gives a very realistic reconstruction of real 3D objects. However, on the heart example (Fig. 11), one can see regularly spaced striations on the volume. These striations are located at the level of the original slices and are due to the fact that the inference calculation is limited to the two enclosing slices with no accounting for further neighbouring sections. A future improvement to the method would be to extend the inference support to several slices.

Acknowledgements

References

[1] A.Rosenfeld and A.C. Kak, *Digital image processing*, Academic Press, New-York, 1982.

[2] G.Borgefors, "Distance transformations in digital images", *CVGIP*, vol. 34, 344-371, 1986.

[3] P.E. Danielsson, "Euclidean distance mapping", *CGIP*, vol. 14, 227-248, 1980.

[4] L. Vincent, "Exact euclidean distance function by chain propagation", *Proc. IEEE of Computer Vision and Pattern Recognition*, Maui, Hawaii, June 3-6, 520-525, 1991.

[5] E. Thiel, A. Montanvert, "Chamfer masks: discrete distance functions, geometrical properties and optimization", *11th Int. Conf. on Pattern Recognition*, The Hague , The Netherlands, August 30-September 3, 244-247, 1992.

[6] C. Arcelli, G. Sanniti di Baja, "Finding local maxima in a pseudo-euclidean distance transform", *CGIP*, vol. 43, 361-367, 1988.

[7] C. Arcelli, G. Sanniti di Baja, "An approach to figure decomposition using width information", *CGIP*, vol. 26, 61-72, 1984.

[8] E. Thiel, A. Montanvert, "Shape splitting from medial lines using the 3-4 chamfer distance", *International Workshop on Visual Form*, May 1991, Capri, published in Plenum Press, New York, 537-546.

[9] Y. Usson, C. Humbert, "Methods for topographical analysis of intra-nuclear BrdUrd-tagged fluorescence", *Cytometry* 13, 595-602, 1992.

[10] F. Parazza, C. Humbert, Y. Usson, "Method for 3D volumetric analysis of intranuclear fluorescence distribution", in press in *Computerized Medical Imaging and Graphics*.

[11] S.B. Ho, C.R. Dyer, "Shape smoothing using medial axis properties", *IEEE tr. on PAMI*, v. 8, 512-520, 1986.

[12] G. Borgefors, "Hierarchical chamfer matching: a parametric edge matching algorithm", *IEEE trans. on PAMI*, vol. 10, 849-865, 1988.

[13] S. Lavallée, R. Szeliski, L. Brunie, "Matching 3D smooth surfaces with their 2D projections using 3D distance maps", *Proc. of SPIE, Geometric Models in Computer Vision*, July 25-26, San Diego, 1991.

[14] G. Borgefors, G. Sanniti di Baja, "Parallel smoothing and decomposition of digital shapes using multiresolution structure", *Proc. 10th Int. Conf. on Pattern Recognition*, Atlantic City, 745-748, 1990.

[15] L. Dorst, I. Mandhyan, K. Trovato, "The geometrical representation of planning problems", *Robotics and Autonumous Synstems*, vol. 7, 181-195, 1991.

[16] M. Coster, J.L. Chermant, *Précis d'analyse d'images*, Presses du CNRS, 1989.

[17] J. Serra, *Image analysis and mathematical morphology*, Academic Press, London, 1989.

[18] H. Fuchs, Z.M. Kedem, S.P. Uselton, "Optimal surface reconstruction from planar contours", *Comm. of ACM*, vol. 20, 693-702, 1977.

[19] J-D. Boissonnat, "Shape reconstruction from planar cross-sections", *CVGIP*, vol. 44, 1-29, 1988.

[20] J-D. Boissonnat, B. Geiger, "Three dimensional reconstruction of complex shapes based on the Delaunay triangulation", *Rapport de Recherche INRIA*, n°1697, May 92.

[21] F. Rolland, A. Montanvert, J-M. Chassery, "Graph matching for 3D reconstruction from cross-sections using simulated annealing", *Proc. of the 7th SCIA*, August 13-16, Aalborg, Denmark, 395-402, 1991.

[22] J-P. Laurent, C. Frendo-Rosso, "Application of image analysis to the estimation of AAC thermal conductivity", *3rd RILEM Int. Symp. on Autoclaved Aerated Concrete*, Zürich, Switzerland, October 14-16, 1992.